AAS 24-423

DERIVATION AND SIMULATION OF USER SCENARIOS FOR LUNAR NAVIGATION SATELLITE SYSTEMS

Mark Hartigan* **and E. Glenn Lightsey†**

Lunar Navigation Satellite Systems (LNSS) are actively being developed by international agencies and private enterprise alike to provide position, navigation, timing, and communications to the growing population of lunar users as the Artemis missions and similar strategies for increasing human presence on the moon come to pass. This work focuses on demonstrating end-user performance for those in low lunar orbit and on the surface. Provided are derivations of dynamics and navigation simulations using various filtering strategies, from pseudorange-based trilateration to unscented Kalman filtering. These strategies are traded and selectively implemented for each user according to achievable accuracy and computational complexity. Ultimately, the unscented Kalman filter yielded the best results for low lunar orbiters, while a linear unbiased minimum variance estimator worked for stationary assets and an extended Kalman filter performed well for astronauts on EVA. The tools developed in this research can be used by LNSS designers to help determine effective constellation capability and can be extended to new use cases and filtering strategies with relative ease.

INTRODUCTION

The creation of lunar navigation satellite systems (LNSS) based on similar Earth-based constellations is an active point of development for international agencies and private enterprise alike. Such systems are necessary to provide position, navigation, timing (PNT), and communications to lunar users – a user base expected to grow in coming years as the Artemis missions and similar strategies for increasing human presence on the moon come to pass. Represented within these missions are a wide range of users with varying requirements for navigation. Any given LNSS design should demonstrate the ability to meet these, especially for critical events such as entry, descent, and landing (EDL) or extra-vehicular activity (EVA) by astronauts.[1] This paper provides derivations and navigation simulations for the use case scenarios of low lunar orbiters and EVA – as well as other likely users – with the objective of providing appropriate tools for evaluating the efficacy of LNSS designs. Different navigation methods are traded for each user, including: pseudorange-based trilateration, *a posteriori* batch estimation, and a variety of real-time Kalman filtering strategies. Measurements from LNSS satellites are assumed to be structured similarly to the spread-spectrum signals broadcast by Earth-based GNSS satellites, as NASA's LunaNet[2] and the ESA's Moonlight Initiative[3] have been targeting. A sample arrangement of satellites in elliptical lunar frozen orbits[4,5] is used as a benchmark for users near the lunar south pole, but this methodology can be extrapolated to other constellation geometries, error budgets, and user locations.

To fully analyze the capabilities of a potential LNSS design, the end-user performance should be comprehensively explored. As such, this paper presents a representative suite of use cases – both

*Graduate Research Assistant, School of Aerospace Engineering, Georgia Institute of Technology, Atlanta, GA.
†John W. Young Chair Professor, School of Aerospace Engineering, Georgia Institute of Technology, Atlanta, GA.

on the lunar surface and in orbit. Users in low lunar orbit exist in highly dynamic environments and typically require real-time results, so a variety of Kalman filtering strategies are explored. Data from NASA's 2009 Lunar Reconnaissance Orbiter mission to the moon[6] is used to provide truth data against which to compare results; it serves as a test case to evaluate filter performance against unmodeled dynamics. This data is also adapted to the scenario of an apolune-raising maneuver, where the Δv is not communicated to the navigation filter – a way to evaluate filter reconvergence after a dynamical disturbance.

Meanwhile, lunar surface users like stationary ground assets, rovers, and astronauts on EVAs are also explored. These users exist in a much less dynamic environment, and may be able to improve their navigation performance using *a posteriori* updates. In the case of an EVA, however, continuous high-accuracy coverage is required for the duration of the event to ensure astronaut safety.[1] Between all these users, the gamut of demanding use cases is surveyed and simulation results will provide system designers with a more complete understanding of LNSS performance.

NASA's LunaNet Interoperability Specifications recommend using spread-spectrum signals modulated with pseudorandom noise codes as the navigation signal broadcast by LNSS designs.[2] This leverages the decades of technological development in GNSS to allow for a scalable system that can be easily improved with more unique satellites. Pseudorange and pseudorange-rate measurements can be derived by the user from these signals, which are implemented for use in the navigation simulations. Uncertainty of these measurements is driven primarily by satellite ephemeris error, clock modeling error, group delays, and user equipment errors. These user scenarios and measurements are fed into some or all of the following filters: a linear unbiased minimum variance estimator (LUMVE), an extended Kalman filter (EKF), and an unscented Kalman filter (UKF). The performance of these filters is explored later in the results section.

METHODOLOGY

Simulations presented in this paper are implemented entirely in MATLAB. General planetary constants and ephemerides are gathered using JPL's SPICE[7,8] application program interface; data for the LRO was retrieved from NASA's Planetary Data System.[9] The apolune-raising maneuver and LNSS orbits were generated using NASA Goddard Space Flight Center's General Mission Analysis Tool (GMAT),[10] then converted into binary ephemeris kernels for integration with SPICE. Overall, dynamics and measurement models for both low lunar orbiters and ground assets making pseudorange and pseudo-range-rate measurements from a hypothetical LNSS constellation are derived; then, constellation geometry and error budgets are adapted from prior work[5] to fit a newer software architecture.

Orbital Dynamics

Traditional Keplerian dynamics describe the motion of a satellite around a primary body using Equation (1):

$$\ddot{\boldsymbol{r}} = -\frac{GM}{r^3}\boldsymbol{r} \tag{1}$$

where $\boldsymbol{r}$ is the position of the satellite w.r.t. the primary body – in our case, the moon. G is the universal gravitational constant and M is the moon's mass; this is often also written using the planet's gravitational parameter $\mu = GM$. In low Earth orbits, the gravitational influence of the moon can be ignored for most use cases as it is relatively much less massive and much further away. This assumption fails in lunar orbits as the Earth's gravitational influence is relatively much larger.

Therefore, (1) can be reformulated to include the influence that the Earth has on both the satellite and the moon[11] (where variables subscripted with s refer to the satellite, $\oplus$ to Earth, and $\mathbb{C}$ to the moon):

$$_{\text{ME}}\ddot{\boldsymbol{r}}_s = -\frac{\mu_{\mathbb{C}}}{r_s^3}\boldsymbol{r}_s + \mu_{\oplus}\left(\frac{\boldsymbol{r}_{\oplus} - \boldsymbol{r}_s}{||\boldsymbol{r}_{\oplus} - \boldsymbol{r}_s||^3} - \frac{\boldsymbol{r}_{\oplus}}{r_{\oplus}^3}\right) \tag{2}$$

But still, Equation (2) does not accurately portray the orbital dynamics of satellites near the moon. The equations thus far make the assumption that each body can be approximated as a point mass (i.e. is a sphere of uniform density); however, both Earth and the moon are not uniform spheres. To account for the nonspherical shape of the primary body and the nonuniform density – and therefore, gravitational field – spherical harmonics are used, discussed in detail in a textbook by Montenbruck and Gill.[11] Rather than using Equation (1), the acceleration of a satellite in orbit around the moon can instead be expressed as:

$$_{\text{ME}}\ddot{\boldsymbol{r}}_s = \nabla\frac{\mu_{\mathbb{C}}}{r_s}\sum_{n=0}^{\infty}\sum_{m=0}^{n}\frac{R_{\mathbb{C}}^n}{r_s^n}P_{nm}(\sin\phi)(C_{nm}\cos m\lambda + S_{nm}\sin m\lambda) \tag{3}$$

where $R_{\mathbb{C}}$ is the reference radius of the moon, P_{nm} is the associated Legendre polynomial of degree n and order m, ϕ and λ are latitude and longitude, and C_{nm} and S_{nm} refer to spherical harmonic coefficients for the moon.[12] This expression is given in the moon body-fixed frame – generally acknowledged as the moon mean-Earth (ME) frame[13] – and must be rotated to the moon-centered inertial frame (ICRF) using the rotation matrix $_{\text{ICRF}}^{\text{ME}}T$. Combining Equations (3) and (2), a set of usable dynamical equations for lunar orbits are generated in Equation (4).

$$\ddot{\boldsymbol{r}}_s = {}_{\text{ICRF}}^{\text{ME}}T\nabla\frac{\mu_{\mathbb{C}}}{r_s}\sum_{n=0}^{N}\sum_{m=0}^{n}\frac{R_{\mathbb{C}}^n}{r_s^n}P_{nm}(\sin\phi)(C_{nm}\cos m\lambda + S_{nm}\sin m\lambda) + \mu_{\oplus}\left(\frac{\boldsymbol{r}_{\oplus} - \boldsymbol{r}_s}{||\boldsymbol{r}_{\oplus} - \boldsymbol{r}_s||^3} - \frac{\boldsymbol{r}_{\oplus}}{r_{\oplus}^3}\right) \tag{4}$$

For computational feasibility, spherical harmonics calculations are truncated to a maximum degree and order N (given that the algorithm is of complexity $\mathcal{O}(N^2)$). As a reference, the initial position and velocity of LRO was taken on October 15, 2009 at midnight and propagated for 24 hours using each of the above methods. These results were then differenced with the true mission data to give a comparison of dynamical model accuracy, plotted in Figure 1.

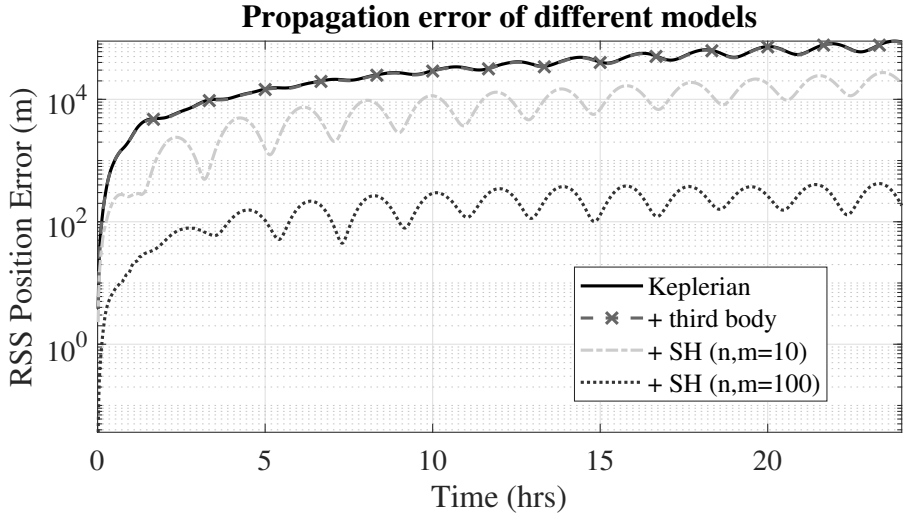

Figure 1: Accuracy of various dynamical models for low lunar orbits, compared with truth data from the LRO mission.[9]

As is evident, using spherical harmonics up to degree and order 100 performs nearly three orders of magnitude better than Keplerian dynamics alone or with third body perturbations over the interval; $N = 100$ also is two orders of magnitude better than only $N = 10$, though the computational cost is much greater.

Letting Equation (4) be $G(\boldsymbol{r}_s, t)$, the satellite dynamics can be represented as

$$\begin{aligned} \boldsymbol{x}_{\text{orb}} &= [\boldsymbol{r}_s \;\; \dot{\boldsymbol{r}}_s]^T \\ \dot{\boldsymbol{x}}_{\text{orb}} &= g(\boldsymbol{x}_{\text{orb}}, t) + \boldsymbol{\varepsilon}_f \\ \begin{bmatrix} \dot{\boldsymbol{r}}_s \\ \ddot{\boldsymbol{r}}_s \end{bmatrix} &= \begin{bmatrix} \dot{\boldsymbol{r}}_s \\ G(\boldsymbol{r}_s, t) \end{bmatrix} + \begin{bmatrix} 0 \\ \boldsymbol{\varepsilon}_{\text{accel}} \end{bmatrix} \end{aligned} \tag{5}$$

where $\boldsymbol{\varepsilon}_{\text{accel}}$ represents the unmodeled errors inherent in Equation (4). For the purposes of this analysis, it is zero-mean Gaussian noise with covariance

$$\text{E}[\boldsymbol{\varepsilon}_{\text{accel}} \boldsymbol{\varepsilon}_{\text{accel}}^T] = Q_{\text{accel}}.$$

Pseudorange and pseudorange-rate measurements are called as such because the receiver's oscillator phase offset and drift add a bias to the measurement (discussed more in detail in the next section). To improve measurement estimates and therefore navigation performance, this information can be tracked within the filter itself. Zucca and Tavella[14] describe oscillators using a random walk- and run-type process model, given by

$$\begin{aligned} \dot{\boldsymbol{x}}_{\text{clk}} &= F\boldsymbol{x}_{\text{clk}} + \boldsymbol{\varepsilon}_{\text{clk}} \\ \begin{bmatrix} \dot{b} \\ a \\ \dot{a} \end{bmatrix} &= \begin{bmatrix} 0 & 1 & 0 \\ 0 & 0 & 1 \\ 0 & 0 & 0 \end{bmatrix} \begin{bmatrix} b \\ \dot{b} \\ a \end{bmatrix} + \boldsymbol{\varepsilon}_{\text{clk}} \end{aligned} \tag{6}$$

$$\text{E}[\boldsymbol{\varepsilon}_{\text{clk}}] = \mathbf{0}_{3\times 1}, \quad \text{E}[\boldsymbol{\varepsilon}_{\text{clk}} \boldsymbol{\varepsilon}_{\text{clk}}^T] = Q_{\text{clk}} = \begin{bmatrix} \sigma_1^2 & 0 & 0 \\ 0 & \sigma_2^2 & 0 \\ 0 & 0 & \sigma_3^2 \end{bmatrix}.$$

Here, $b = c \cdot \delta t$ is the oscillator phase offset, $\dot{b} = c \cdot \delta \dot{t}$ is the phase drift or frequency offset, and a is the frequency drift or aging rate. σ_1, σ_2, and σ_3 are parameters relating to the Allan or Hadamard variance of the oscillator (a Microchip Space CSAC[15] is baselined); further information can be found in Zucca and Tavella's paper.[14]

Equations (5) and (6) can be combined to arrive at the final dynamical representation of the system:

$$\dot{\boldsymbol{x}} = f(\boldsymbol{x}, t) + \boldsymbol{\varepsilon}, \quad \boldsymbol{x} = [\boldsymbol{x}_{\text{orb}} \;\; \boldsymbol{x}_{\text{clk}}]^T \tag{7}$$

$$\begin{bmatrix} \dot{\boldsymbol{r}}_s \\ \ddot{\boldsymbol{r}}_s \\ \dot{b} \\ a \\ \dot{a} \end{bmatrix} = \begin{bmatrix} \dot{\boldsymbol{r}}_s \\ G(\boldsymbol{r}_s, t) \\ \dot{b} \\ a \\ 0 \end{bmatrix} + \begin{bmatrix} 0 \\ \boldsymbol{\varepsilon}_{\text{accel}} \\ \boldsymbol{\varepsilon}_{\text{clk}} \end{bmatrix}$$

Of importance for propagating uncertainty within the filters is the jacobian of f w.r.t. $\boldsymbol{x}$. Due to the complexity of the dynamics in (3), the spherical harmonics of the moon are approximated as only J_2 for the purposes of this calculation. The acceleration on the satellite due to the J_2 effect in the moon ME frame can be written as

$${}_{\text{ME}}\ddot{\boldsymbol{r}}_s = \frac{3C_{2,0}\mu_{\text{☾}}R_{\text{☾}}^2}{2r_s^4} \begin{bmatrix} \left(1 - 5\left(\frac{z}{r_s}\right)^2\right)\frac{x}{r_s} \\ \left(1 - 5\left(\frac{z}{r_s}\right)^2\right)\frac{y}{r_s} \\ \left(3 - 5\left(\frac{z}{r_s}\right)^2\right)\frac{z}{r_s} \end{bmatrix}, \quad \boldsymbol{r}_s = [x \;\; y \;\; z]^T.$$

From here, the jacobian $A = \frac{\partial f}{\partial \boldsymbol{x}}$ can be solved for.

$$A = \begin{bmatrix} \mathbf{0}_{3\times3} & \boldsymbol{I}_{3\times3} & \mathbf{0}_{3\times3} \\ \frac{\partial g}{\partial \boldsymbol{x}} & \mathbf{0}_{3\times3} & \mathbf{0}_{3\times3} \\ \mathbf{0}_{3\times3} & \mathbf{0}_{3\times3} & F \end{bmatrix} \tag{8}$$

Equation (8) will be used by the filtering algorithms later.

Surface Dynamics

The second group to examine are surface users: namely, stationary ground assets, rovers, and astronauts on EVAs. This group is characterized by low relative dynamics and general operation in a moon-fixed frame. Stationary assets in particular should be able to obtain high-accuracy position estimates over long time periods using *a posteriori* estimation strategies. The modeling for simulations is trivial, as the asset occupies a chosen fixed point on the lunar surface in the moon-fixed frame from which measurements can be computed.

Accurate modeling of the lunar surface is achievable thanks to the Lunar Orbiter Laser Altimeter (LOLA) onboard the Lunar Reconnaissance Orbiter, and Barker et al.[16] for performing the data post-processing. This dataset consists of a two-dimensional array of surface elevations w.r.t. the reference sphere ($r = 1737.4$ km) in stereographic coordinates. A surface point, referenced via latitude and longitude, can be converted into stereographic coordinates to obtain elevation. Then,

converting back to latitude / longitude and using spherical to cartesian conversions yields the position in the moon-fixed frame. These conversions are

$$\begin{bmatrix} x \\ y \end{bmatrix} = \begin{bmatrix} R\sin\lambda \\ R\cos(\lambda) \end{bmatrix}, \quad R = 2r\tan\left(\frac{1}{2}(\frac{\pi}{2} - |\phi|)\right)\text{sign}(\phi)$$

$$\boldsymbol{x}_{ME} = (r + \text{elev}(x, y)) \begin{bmatrix} \cos\lambda\sin\phi \\ \sin\lambda\sin\phi \\ \cos\phi \end{bmatrix}.$$

An elevation map of the lunar south pole taken from this data is shown in Figure 2.

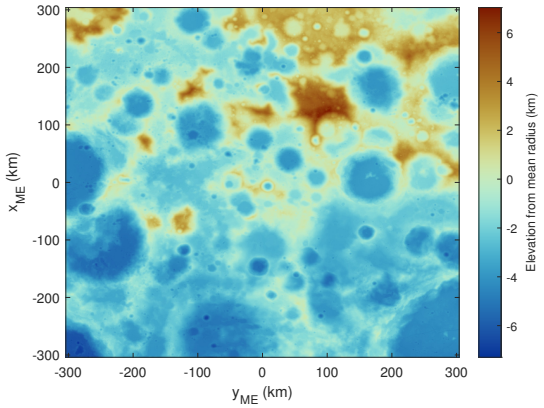

Figure 2: Elevation map of the lunar south pole up to roughly $80°$S.[16] The top of the image is $0°$ longitude, and the right is $90°$E.

For moving users, a scheme needs to be laid out to construct appropriate and representative trajectories. Rovers and astronauts on EVAs will likely not be idly wandering – rather, it may more resemble point-to-point travel between tasks or points of scientific interest, navigating around obstacles *en route* and dwelling at each point to complete some objective. As such, modular trajectory generation functionality was created to allow flexibility in waypoints, average travel speed, region of operation, and task length. The shortest straight-line paths between waypoints – comprising a latin hypercube sample of the operating region – are generated using true elevation data. Deviations are then added to this path to simulate obstacle avoidance and the paths are interpolated using piecewise cubic hermite splines. A sample trajectory is shown in Figure 3a, which represents an astronaut traveling between four objectives and home base on EVA. Each parameter can be adjusted as desired to yield a trajectory representative of the target use case.

Each segment of the piecewise polynomial comprising the user's trajectory is a cubic hermite spline, allowing for continuous first and second derivatives. Equation (9) gives the form these polynomials adopt:

$$\boldsymbol{x}(t) = \begin{bmatrix} \alpha_{3,i}t^3 + \alpha_{2,i}t^2 + \alpha_{1,i}t + \alpha_{0,i} \\ \beta_{3,i}t^3 + \beta_{2,i}t^2 + \beta_{1,i}t + \beta_{0,i} \\ \gamma_{3,i}t^3 + \gamma_{2,i}t^2 + \gamma_{1,i}t + \gamma_{0,i} \end{bmatrix}, \quad t \in [t_i, t_{i+1}] \tag{9}$$

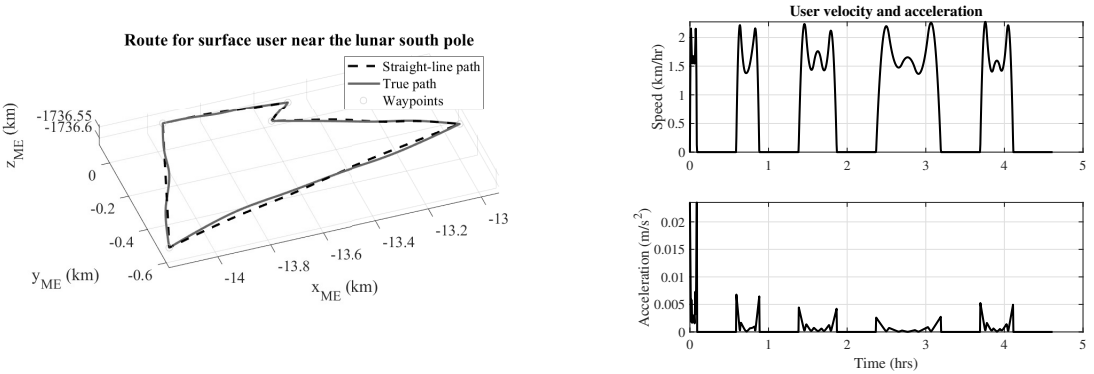

(a) Trajectory across surface

(b) Speed and acceleration over time

Figure 3: Sample trajectory for an astronaut conducting EVA.

The velocity and acceleration can then be found through simple differentiation.

$$\dot{\boldsymbol{x}}(t) = \frac{d}{dt}\boldsymbol{x}(t) = \begin{bmatrix} 3\alpha_{3,i}t^2 + 2\alpha_{2,i}t + \alpha_{1,i} \\ 3\beta_{3,i}t^2 + 2\beta_{2,i}t + \beta_{1,i} \\ 3\gamma_{3,i}t^2 + 2\gamma_{2,i}t + \gamma_{1,i} \end{bmatrix}, \quad t \in [t_i, t_{i+1}] \tag{10}$$

$$\ddot{\boldsymbol{x}}(t) = \frac{d^2}{dt^2}\boldsymbol{x}(t) = \begin{bmatrix} 6\alpha_{3,i}t + 2\alpha_{2,i} \\ 6\beta_{3,i}t + 2\beta_{2,i} \\ 6\gamma_{3,i}t + 2\gamma_{2,i} \end{bmatrix}, \quad t \in [t_i, t_{i+1}] \tag{11}$$

Thus, the velocity and accelerations over time in Figure 3b are obtained. The 30-minute periods of no movement represent the astronaut performing tasks as the given location, while between points they average 1.6 km/hr at a walking pace.

Using this structure, the dynamics for use in navigation filters can be derived in Equation (12):

$$\dot{\boldsymbol{x}}(t) = \begin{bmatrix} 0_{3\times3} & I_{3\times3} & 0_{3\times3} \\ 0_{3\times3} & 0_{3\times3} & 0_{3\times3} \\ 0_{3\times3} & 0_{3\times3} & F \end{bmatrix} \boldsymbol{x}(t) + \begin{bmatrix} 0_{3\times3} \\ I_{3\times3} \\ 0_{3\times3} \end{bmatrix} \boldsymbol{a}(t) + \begin{bmatrix} 0 \\ \boldsymbol{\varepsilon}_{\text{accel}} \\ \boldsymbol{\varepsilon}_{\text{clk}} \end{bmatrix}. \tag{12}$$

As the application here is for real-time navigation filters which assume the use of an accelerometer, discretized dynamics can be used between accelerometer updates for simplicity. In this case, $\boldsymbol{\varepsilon}_{\text{accel}}$ can be considered a zero-mean Gaussian noise with covariance Q_{accel}.

Measurement Model

NASA's current lunar interoperability specifications[2] target a passive system like terrestrial GNSS, wherein signals are broadcast with a specific structure such that any user capable of receiving the signals can use information encoded within to make estimates of the range between them and the broadcasting satellite, called *pseudoranges*. Higher-end receivers also track the signal Doppler shift, which can be used to estimate the range-rate between user and satellite (*pseudorange-rate*). These measurements are formulated in Equations (13) and (14).

$$\rho(t) = ||\boldsymbol{r}_i(t-\tau) - \boldsymbol{r}_s(t)|| + b + \varepsilon_\rho(t) \tag{13}$$

$$\hat{\boldsymbol{u}}_i = \frac{\boldsymbol{r}_i(t-\tau) - \boldsymbol{r}_s(t)}{||\boldsymbol{r}_i(t-\tau) - \boldsymbol{r}_s(t)||}$$
$$\dot{\rho}(t) = [\dot{\boldsymbol{r}}_i(t-\tau) - \dot{\boldsymbol{r}}_s(t)] \cdot \hat{\boldsymbol{u}}_i + \dot{b} + \varepsilon_{\dot{\rho}}(t) \tag{14}$$

Here, $\boldsymbol{r}_i$ refers to the position of the i-th LNSS satellite in view and ε_ρ, $\varepsilon_{\dot{\rho}}$ are the associated measurement errors (discussed later). The measurements obtained by the user at a given time t from M satellites are then written as

$$\boldsymbol{y}(t) = h(\boldsymbol{x}, t) = \begin{bmatrix} \rho_1(t) & \dots & \rho_M(t) & \dot{\rho}_1(t) & \dots & \dot{\rho}_M(t) \end{bmatrix}^T. \tag{15}$$

The jacobian of (15), used by navigation filters, then becomes

$$H = \frac{\partial h}{\partial \boldsymbol{x}} = \begin{bmatrix} \frac{-(\boldsymbol{r}_1 - \boldsymbol{r}_s)^T}{||\boldsymbol{r}_1 - \boldsymbol{r}_s||} & 0 & 1 & 0 & 0 \\ & \dots & & & \\ \frac{-(\boldsymbol{r}_M - \boldsymbol{r}_s)^T}{||\boldsymbol{r}_M - \boldsymbol{r}_s||} & 0 & 1 & 0 & 0 \\ \frac{((\boldsymbol{r}_1 - \boldsymbol{r}_s)\cdot(\dot{\boldsymbol{r}}_1 - \dot{\boldsymbol{r}}_s))(\boldsymbol{r}_1 - \boldsymbol{r}_s)^T}{||\boldsymbol{r}_1 - \boldsymbol{r}_s||^3} - \frac{(\dot{\boldsymbol{r}}_1 - \dot{\boldsymbol{r}}_s)^T}{||\boldsymbol{r}_1 - \boldsymbol{r}_s||} & \frac{-(\boldsymbol{r}_1 - \boldsymbol{r}_s)^T}{||\boldsymbol{r}_1 - \boldsymbol{r}_s||} & 0 & 1 & 0 \\ & \dots & & & \\ \frac{((\boldsymbol{r}_M - \boldsymbol{r}_s)\cdot(\dot{\boldsymbol{r}}_M - \dot{\boldsymbol{r}}_s))(\boldsymbol{r}_M - \boldsymbol{r}_s)^T}{||\boldsymbol{r}_M - \boldsymbol{r}_s||^3} - \frac{(\dot{\boldsymbol{r}}_M - \dot{\boldsymbol{r}}_s)^T}{||\boldsymbol{r}_M - \boldsymbol{r}_s||} & \frac{-(\boldsymbol{r}_M - \boldsymbol{r}_s)^T}{||\boldsymbol{r}_M - \boldsymbol{r}_s||} & 0 & 1 & 0 \end{bmatrix}. \tag{16}$$

LNSS Satellites

NASA has been the primary requirements driver for cislunar PNT constellations, as it plays a key part in supporting ground users for future Artemis missions. Most of these requirements are captured in the LunaNet Interoperability Specifications,[2] which call for the PNT portion of the constellation to act much the same as terrestrial GNSS. The defined Initial Operating Capability (which lasts until 2030 at the earliest) targets the lunar south pole as its service volume. As such, most preliminary designs focus on elliptical lunar frozen orbits (ELFOs)[17] with apolune over the south pole due to their natural stability resulting in reduced stationkeeping costs.

Constellation Geometry The geometry used here was discussed at length in prior work[5] and is adapted from a constellation of eight satellites conceived by Murata et al.[18] Their work used two ELFOs separated by a right ascension of $180°$; in one, each satellite is at a true anomaly of $90i°$, $i = 0, 1, 2, 3$ and in the other $(45 + 90i)°$, $i = 0, 1, 2, 3$. The selected orbits have a semimajor axis of 6541.4 km, eccentricity of 0.6, inclination of $56.2°$, and argument of perilune of $90°$. This was then optimized for coverage of the lunar south pole by adjusting relative true anomalies within the orbital planes, eventually arriving at the geometry pictured in Figure 5.

Measurement Accuracy NASA provides requirements for any Lunar Relay Service Provider,[1] which constrains the signal-in-space errors (SISE) of the service to those listed in Table 4.

Error	Value
SISE Position	13.43 m (3-sigma)
SISE Velocity	1.2 mm/s (3-sigma) @ 10 sec

Figure 4: Lunar Relay PNT reference signal source SISE requirements.[1]

The measurement uncertainty in Equations (13) and (14) is approximated as zero-mean Gaussian

noise with the following covariance:

$$\begin{aligned} \mathrm{E}[\varepsilon_\rho \varepsilon_\rho^T] &\approx \mathrm{SISE}_{\mathrm{pos}}^2 + \mathrm{UEE}_{\mathrm{pos}}^2 = R_1 = (5\ \mathrm{m})^2 \\ \mathrm{E}[\varepsilon_{\dot\rho} \varepsilon_{\dot\rho}^T] &\approx \mathrm{SISE}_{\mathrm{vel}}^2 + \mathrm{UEE}_{\mathrm{vel}}^2 = R_2 = (0.9\ \mathrm{mm/s})^2 \end{aligned} \tag{17}$$

For this paper, the user equipment errors $\mathrm{UEE}_{\mathrm{pos}}$ and $\mathrm{UEE}_{\mathrm{vel}}$ are assumed to be 0.5 meters 1σ and 0.5 mm/s 1σ, respectively.

SIMULATION SETUP

In this section, detailed descriptions of two LLO and two surface user scenarios are provided; the filtering methods to be explored are then reviewed.

User Scenarios

Low Lunar Orbiters While LLO users are not the primary target of LunaNet's Initial Operating Capability, they can still benefit from the measurements being provided by LNSS satellites. As such, two cases will be examined; first, a high-fidelity trajectory from the Lunar Reconnaissance Orbiter.[6] This mission data was taken from NASA's PDS archives,[9] which provides the entire postprocessed trajectory of the spacecraft. As evident from Figure 1, very high-order gravity models are required to accurately estimate the dynamics in such low orbits. This case will test each filter's ability to compensate for unmodeled effects. Second, the starting state of the LRO was taken and propagated in GMAT using a lower-order gravity model (N=10) but an orbit-raising maneuver (100 m/s Δv in the velocity direction) was added six hours in. This maneuver is not communicated to the filter so that its reconvergence after a disturbance can be tested. Figure 5 gives propagations of each case over 24 and 12 hours, respectively. The starting epochs of these propagations were chosen to fall within the nominal mission timeline of LRO, and some liberties were taken to assume the LNSS satellites were in orbit at this time.

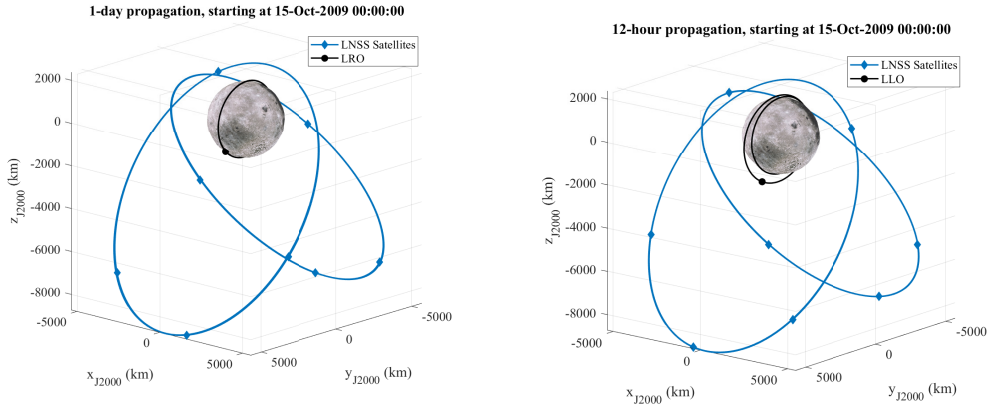

(a) Lunar Reconnaissance Orbiter

(b) Low Lunar Orbiter

Figure 5: Propagation of orbits over the evaluation windows, with final positions of every satellite given by the markers.

It is assumed that the only navigation equipment these spacecraft have is an appropriate radiofrequency receiver to track the LNSS satellites – similar to spaceborne GNSS receivers in use today.

Spacecraft typically have other navigational aids such as star trackers or inertial navigation systems, but this assumption allows for direct testing of LNSS signal quality and availability without overestimating equipment available to the user, since a wide variety of users will be navigating with this constellation. The oscillator for each receiver was modeled as a Microchip Space CSAC,[15] which allowed for Q_{clk} parameters to be derived. Pseudorange and pseudorange-rate measurements are taken once per minute from any visible satellites to the user (i.e. not obstructed by the moon and within the assumed 30° half-angle beamwidth of the LNSS antennae, outside of which the signal to noise density ratio would be too poor for users to acquire a lock). There is also no carrier smoothing of code measurements, so the pseudorange error is as described in Equation (17). All filters for the LRO case will use a gravity model up to degree and order 100, while the second case uses up to 10 (perfect knowledge of the dynamics for that case).

Surface Users The first of two surface users considered is a ground asset that is stationary in the moon-fixed frame at -89.5° latitude, 180° longitude (The moon ME frame orientation w.r.t. an ICRF inertial frame can be obtained using SPICE). This asset will be making pseudorange and -range-rate measurements at 0.1 Hz from all available satellites for four hours. The second user will be an astronaut out on EVA within a 1-km radius of -89.5° latitude, 0° longitude, making similar measurements at 0.1 Hz. NASA's Lunar Relay Services Requirements carve out four hours for EVA with one hour of contingency,[1] so the EVA will last 4 hours. For inclusion in navigation filters, the astronaut's equipment will include a low-cost COTS accelerometer – specifications of Analog Devices, Inc.'s AXDL359 are used for these simulations.[19] The accelerometer is being sampled for state propagation purposes at 1 Hz. A sample trajectory is displayed in Figure 3. The astronaut will visit four waypoints then return to base, staying at each waypoint for 30 minutes and traveling between them at an average of 1.6 km/hr. All waypoints lie within a 1-km radius.

Filtering Methods

Each user scenario is tested using pseudorange-based trilateration, a linear unbiased minimum variance estimator, an extended Kalman filter, and/or an unscented Kalman filter. Dynamics are approximate in the LRO and surface user cases and exact in the LLO case (but without knowledge of any maneuvers). Dynamics and their partials are provided by Equations (7), (8), and (12); the measurement model and its partials are given by (15) and (16). Process noise becomes

$$Q = \begin{bmatrix} \mathbf{0}_{3\times3} & \mathbf{0}_{3\times3} & \mathbf{0}_{3\times3} \\ \mathbf{0}_{3\times3} & Q_{\text{accel}} & \mathbf{0}_{3\times3} \\ \mathbf{0}_{3\times3} & \mathbf{0}_{3\times3} & Q_{\text{clk}} \end{bmatrix}.$$

For the low lunar orbiters Q_{accel} is determined experimentally to be

$$Q_{\text{accel}} = \left(\frac{3}{N} * 10^{-5}\right)^2 \cdot I_3.$$

For surface users carrying an accelerometer, it becomes

$$Q_{\text{accel}} = \sigma_{\text{IMU}}^2 \cdot I_3.$$

The ADXL359 used in this paper has an accuracy around $\sigma_{\text{IMU}} = 80\mu g$ at 1 Hz.[19] Measurement noise can be written using Equation (17) as

$$R = \begin{bmatrix} R_{1,1} & 0 \\ \dots & \dots \\ R_{1,M} & 0 \\ 0 & R_{2,1} \\ \dots & \dots \\ 0 & R_{2,M} \end{bmatrix}$$

RESULTS

Low Lunar Orbiters

For both the case of LRO and the LLO, the LNSS satellites visible to each user are plotted in Figure 6. There are a few brief moments during which all eight satellites are in view; however, there is a general two-hour periodic trend of going from no satellites in view, to six satellites in view, and back down to no satellites in view. Generally, the quality of position and velocity measurements are directly correlated with number of satellites, so there will be evident peaks and valleys throughout the navigation simulations that line up with these visibility trends.

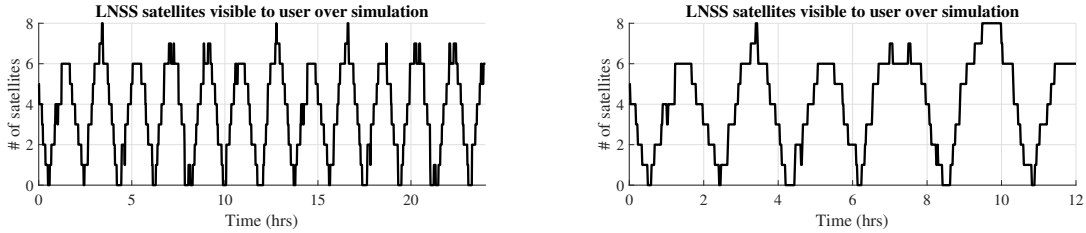

(a) Lunar Reconnaissance Orbiter (b) Low Lunar Orbiter

Figure 6: Visible LNSS satellites to each user over the interval.

The extended Kalman filter performance for both cases can be found in Figure 7. Trends of peaks and valleys that correspond inversely with the number of visible satellites are obvious. Looking at the LRO plot on the left, the filter maintains an average position uncertainty of 4.3 meters (median 1.5 meters). The 3σ bounds fit reasonably well for the case of the LRO; however, looking over to the case including a maneuver, there is a large discrepancy immediately post-maneuver at 6 hours. This is due to the filter not being informed of the Δv, so it still assumes it has a reasonable knowledge of the dynamics – better than it actually does. This case has an average position error of 102 meters, with a median of 2.2 meters. After the maneuver, it takes the filter 1.4 hours to drop back under 10 meters. The cases took 81.7 and 6.9 seconds to run, respectively.

Overall the EKF displays an excellent ability to track the state when the dynamics are well-known and undisturbed, though it struggles to reconverge after an unmodeled disturbance. Faster convergence was displayed when the process noise was higher, though the steady-state error was also higher. Both algorithms executed relatively quickly and would be suitable for real-time applications.

Next, Figure 8 displays the same simulation but with an unscented Kalman filter. Overall the performance appears very similar to the EKF; the LRO case yielded an average position error of

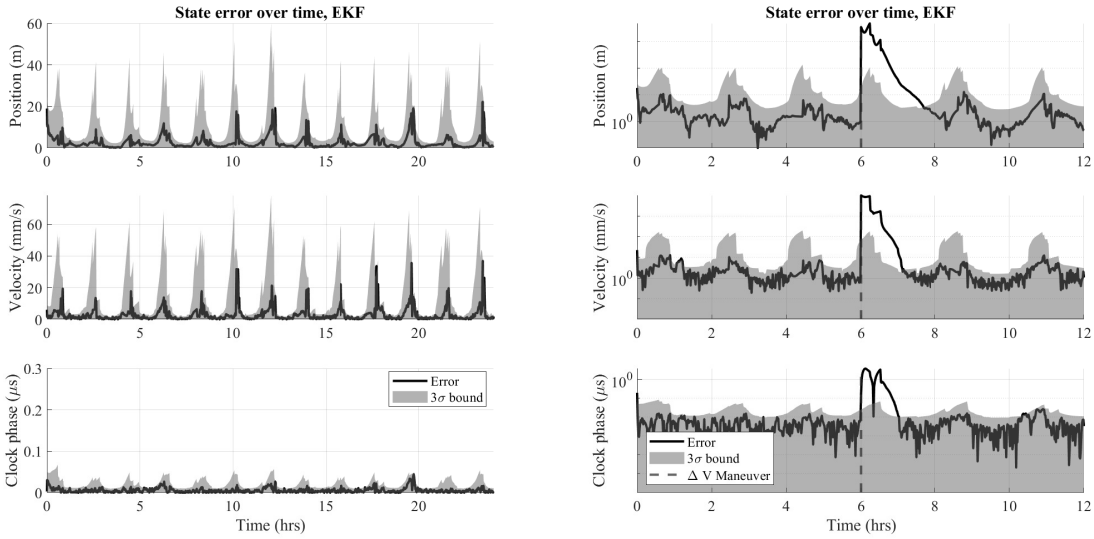

(a) Lunar Reconnaissance Orbiter

(b) Low Lunar Orbiter

Figure 7: State error w.r.t. truth of an extended Kalman filter ($N_{\text{sph}} = 100$).

2.7 meters (median 1.7 meters). The lower mean and similar median indicates the UKF is slightly better at appropriately propagating the state when measurements are infrequent / unavailable. For the maneuver, the average error was 88.4 meters with a median of 2.1, corroborating the results from the previous case. It also took just 1 hour to return under 10 meters post-maneuver, representing a slight improvement over the EKF results. Execution time was 1520 and 69.1 seconds each.

The UKF saw better performance during periods of low or no measurements; this is because the unscented transformation and propagation of points better captures the unmodeled dynamics in low lunar orbit. It also returns from a disturbance slightly quicker, likely thanks to its propagation and evaluation of measurements at multiple points. However, runtime increased by an order of magnitude because 18 points are now being propagated at each time step, rather than just one. Depending on the flight computer, this may still be feasible to execute onboard, and proves to yield navigation performance improvements for critical applications.

Table 1: Navigation performance statistics [mean (3σ), median (3σ)] for the orbital users.

Filter	Position Error (m)	Velocity Error (mm/s)	Phase Error (ns)	Exec.
EKF, LRO	4.31 (11.1), 1.46 (5.66)	3.02 (15.8), 1.60 (6.30)	5.18 (21.6), 3.27 (15.6)	81.7s
UKF, LRO	2.72 (10.8), 1.74 (5.54)	3.16 (15.8), 1.57 (6.32)	5.28 (21.4), 3.85 (15.4)	1520s
EKF, Δv	102 (19.1), 2.20 (6.05)	229 (32.9), 1.75 (5.26)	110 (24.4), 4.18 (15.5)	6.90s
UKF, Δv	88.4 (17.9), 2.08 (5.37)	215 (32.7), 1.66 (5.26)	143 (23.5), 3.74 (14.6)	69.1s

Ultimately, both filters were able to meet the navigation requirements for each scenario imposed by NASA's Lunar Relay Services.[1] An excerpt of these requirements are provided in Figure 9; for low lunar orbiters such as these, a position error less than 100 meters and velocity error less than 10 mm/s (each 3σ) is required and met.

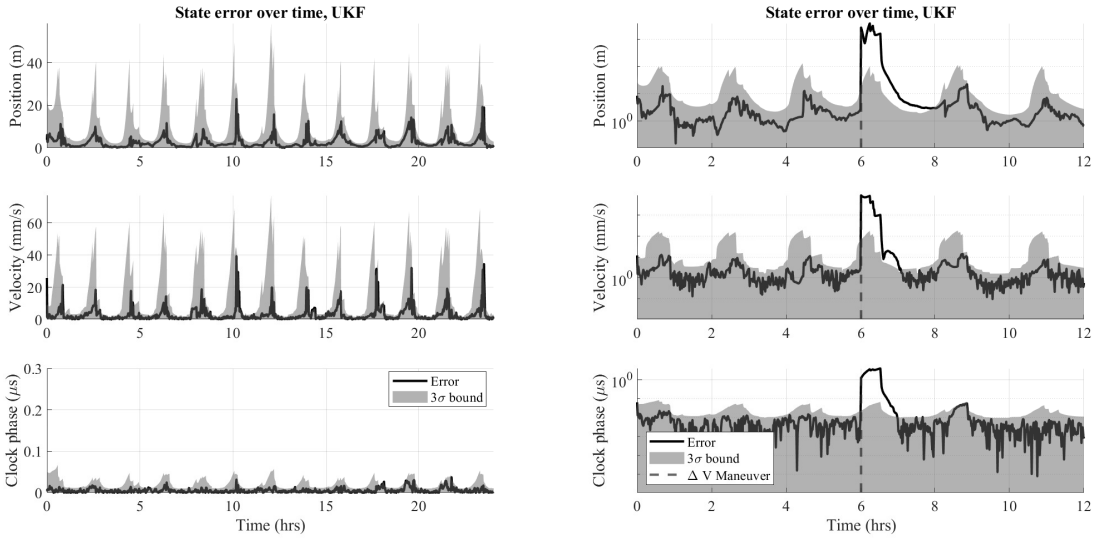

(a) Lunar Reconnaissance Orbiter

(b) Low Lunar Orbiter

Figure 8: State error w.r.t. truth of an unscented Kalman filter ($N_{\text{sph}} = 100$).

	Lander/Orbiter - Low Lunar Orbit	Lander - Prior to De-Orbit Insertion	Powered Descent Initiation to Landing	General Surface
Position Knowledge (m) (3-sigma value)	100	100	25 radius[1]	± 10 absolute; < 10 relative[2]
Velocity Knowledge (m/s) (3-sigma value)	0.01	0.05	0.1 3D[3]	N/A[4]

Figure 9: Lunar Relay representative user scenario performance requirements.[1]

Surface Users

Both the ground station and astronaut operated relatively close to the lunar south pole. Because of this, the visible satellites were nearly identical (only one plot is provided in Figure 10 for brevity). Consequently, the GDOP and eventual navigation errors seen were nearly identical. Figure 10b plots trilateration results for the EVA, though the ground station results look the same. Since navigation error using this method is simply the product of (17) and GDOP, the correlation between the two plots on the right make intuitive sense. In more realistic scenarios, the measurements would not be zero-mean and normally distributed as they are here; this is due to assumptions made about the measurement noise in prior sections. Unfortunately, multilateration proves insufficient on its own to meet the NASA positioning requirements for ground users of 10 meters 3σ, shown in Figure 9.

To remedy this issue for stationary users, a relatively simple batch filter is implemented in the form of a LUMVE. The fixed position allows for easy synthesis of measurements from different points in time, refining the solution beyond the results in Figure 10. Figure 11 shows the results from 4 hours of measurements (10 seconds apart); the left used only pseudoranges, while the right

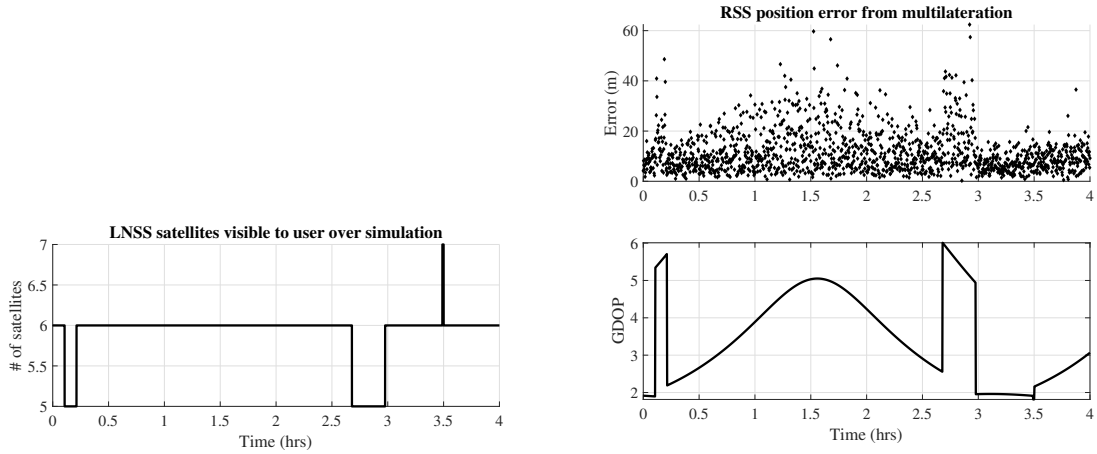

(a) Visible satellites

(b) Trilateration performance

Figure 10: Pseudorange-based multilateration results for surface users near the south pole.

also included pseudorange-rates. As is evident from the plots, the user is able to converge to a more precise solution when considering range-rates, even while stationary. However, the inclusion of these measurements is predicated on having an advanced receiver.

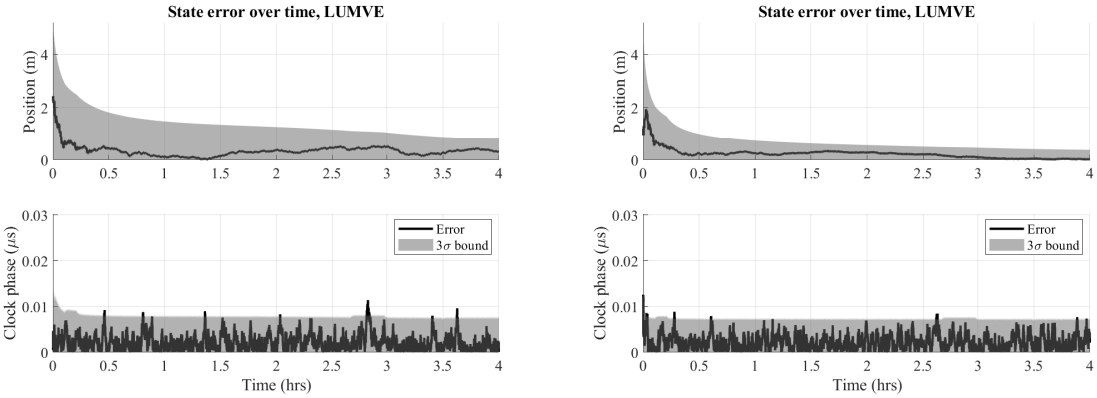

(a) Ranging only

(b) Range and range-rate

Figure 11: Ground station navigating via a LUMVE with different observables.

Unfortunately LUMVEs are not quite so useful for astronauts or rovers needing real-time solutions; additionally, their complex and sometimes erratic movements make it difficult to propagate measurements through time for comparison. In this case, EKFs as shown in Figure 12 may prove more useful. These results show more fluctuation than the ground station due to the motion of the astronaut but remain within reasonable bounds for the duration of the EVA. The navigation solution is also greatly improved by the inclusion of pseudorange-rate measurements (shown on the right).

Table 2 lists the statistical performance of each navigation filter. All users, even without the inclusion of range-rate measurements, were able to meet the 10-meter positioning requirement;

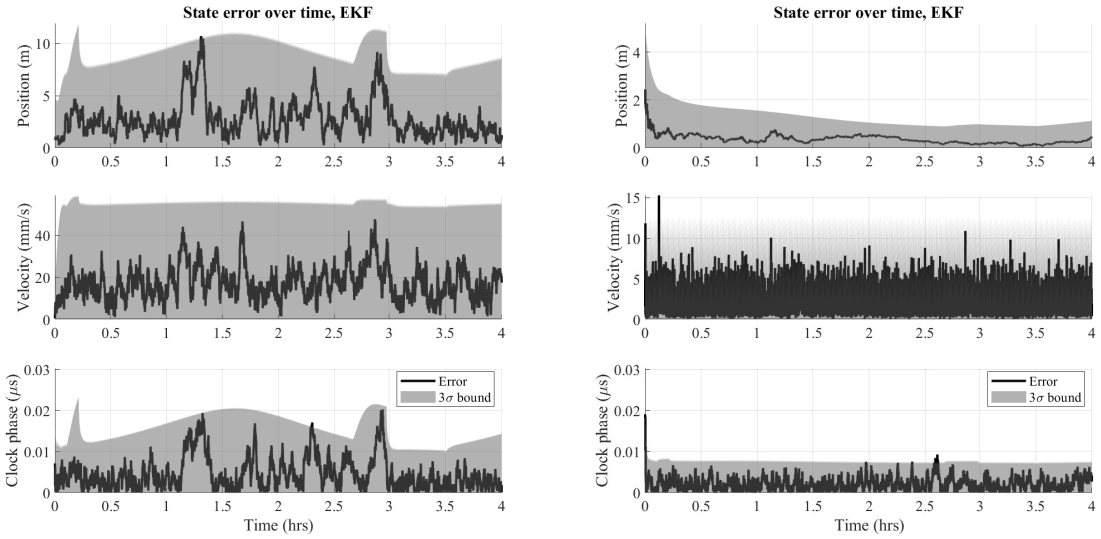

(a) Ranging only

(b) Range and range-rate

Figure 12: Astronaut on EVA navigating via an EKF with different observables.

though for users looking for more accurate results they are a helpful inclusion.

Table 2: Navigation performance statistics [mean (3σ), median (3σ)] for the surface users.

Filter	Position Error (m)	Velocity Error (mm/s)	Phase Error (ns)
LUMVE (ρ), GS	0.34 (1.4), 0.33 (1.27)	-	2.16 (7.89), 1.75 (7.78)
LUMVE (ρ, $\dot{\rho}$), GS	0.18 (0.70), 0.13 (0.56)	-	0.34 (1.66), 0.25 (1.42)
EKF (ρ), EVA	2.77 (8.98), 2.36 (8.84)	17.6 (54.9), 16.6 (55.1)	4.51 (15.5), 3.40 (15.1)
EKF (ρ, $\dot{\rho}$), EVA	0.360 (1.31), 0.33 (1.09)	2.63 (8.38), 2.40 (9.28)	2.15 (7.55), 1.87 (7.51)

CONCLUSIONS

In summary, achievable navigation performance for users on the surface and in low lunar orbit of a potential LNSS constellation was explored. User dynamics and measurement models were created, with derivations, and compared against real mission data for accuracy. Realistic LNSS performance metrics were obtained from NASA requirements documents and simulated, along with the user, in four different user navigation scenarios. The performance of various filtering strategies for each scenario was compared; overall, the UKF provided the most accurate results for LLO users, though the EKF was the fastest by an order of magnitude. Reduced computational expense could be possible with minimal impact on performance by only using an unscented transformation w.r.t. position and velocity, as the clock parameters are relatively well modeled. A LUMVE proved sufficient for stationary ground assets, while astronauts on EVA benefitted from the real-time nature of an EKF. For all users, strictly using the results derived from trilateration performed much worse and violated requirements laid out by NASA for performance. This paper provides a solid framework on which different LNSS designs can be evaluated to consider the end-user navigation performance

possible. This methodology can be extended to different user scenarios or filtering algorithms as needed.

REFERENCES

[1] N. Speciale, "Lunar Relay Services Requirements Document (SRD)," Requirements Document ESC-LCRNS-REQ-0090, NASA, Goddard Space Flight Center, Dec. 2022.

[2] N. Babu, "LunaNet Interoperability Specification Document," Sept. 2022.

[3] P. Giordano, F. Malman, R. Swinden, P. Zoccarato, and J. Ventura-Traveset, "The Lunar Pathfinder PNT Experiment and Moonlight Navigation Service: The Future of Lunar Position, Navigation and Timing," Long Beach, California, Feb. 2022, pp. 632–642, 10.33012/2022.18225.

[4] T. A. Ely and E. Lieb, "Constellations of elliptical inclined lunar orbits providing polar and global coverage," *The Journal of the Astronautical Sciences*, Vol. 54, Mar. 2006, pp. 53–67, 10.1007/BF03256476.

[5] M. Hartigan, D. Smith, and E. G. Lightsey, "Optimization of Early-Phase Cislunar Navigation Constellations for Users Near the Lunar South Pole," *Advances in the Astronautical Sciences*, Big Sky, MT, USA, Univelt, Inc., Aug. 2023.

[6] C. R. Tooley, M. B. Houghton, R. S. Saylor, C. Peddie, D. F. Everett, C. L. Baker, and K. N. Safdie, "Lunar Reconnaissance Orbiter Mission and Spacecraft Design," *Space Science Reviews*, Vol. 150, Jan. 2010, pp. 23–62, 10.1007/s11214-009-9624-4.

[7] C. H. Acton, "Ancillary data services of NASA's Navigation and Ancillary Information Facility," *Planetary and Space Science*, Vol. 44, Jan. 1996, pp. 65–70, 10.1016/0032-0633(95)00107-7.

[8] C. Acton, N. Bachman, B. Semenov, and E. Wright, "A look towards the future in the handling of space science mission geometry," *Planetary and Space Science*, Vol. 150, Jan. 2018, pp. 9–12, 10.1016/j.pss.2017.02.013.

[9] J. Burtnick, D. Myers, N. Castro, L. Tornabene, D. Waters, R. Saylor, R. Casasanta, and W. Calk, "Lunar Reconnaissance Orbiter SPICE Kernels V1.0," , 10.17189/1520116

[10] S. Hughes, D. Conway, and J. Parker, "Using the General Mission Analysis Tool (GMAT)," Breckenridge, CO, Feb. 2017. Publisher: Unpublished, 10.13140/RG.2.2.12685.54249.

[11] O. Montenbruck and E. Gill, *Satellite orbits: models, methods, and applications*. Berlin : New York: Springer, 2000.

[12] A. S. Konopliv, A. B. Binder, L. L. Hood, A. B. Kucinskas, W. L. Sjogren, and J. G. Williams, "Improved Gravity Field of the Moon from Lunar Prospector," *Science*, Vol. 281, Sept. 1998, pp. 1476–1480, 10.1126/science.281.5382.1476.

[13] B. Archinal, C. Fassett, L. Gaddis, T. Hare, E. Malaret, L. Ostrach, and R. Park, "Continued Use of the Mean Earth (ME) Coordinate System for the Moon," tech. rep., Universities Space Research Association, Lunar and Planetary Institute, Sept. 2023.

[14] C. Zucca and P. Tavella, "The clock model and its relationship with the Allan and related variances," *IEEE Transactions on Ultrasonics, Ferroelectrics and Frequency Control*, Vol. 52, Feb. 2005, pp. 289–296, 10.1109/TUFFC.2005.1406554.

[15] "Space CSAC," Datasheet SA.45s, Microchip, Mar. 2019.

[16] M. K. Barker, E. Mazarico, G. A. Neumann, D. E. Smith, M. T. Zuber, J. W. Head, and X. Sun, "A New View of the Lunar South Pole from the Lunar Orbiter Laser Altimeter (LOLA)," *The Planetary Science Journal*, Vol. 4, Sept. 2023, p. 183, 10.3847/PSJ/acf3e1.

[17] T. A. Ely, "Stable Constellations of Frozen Elliptical Inclined Lunar Orbits," *The Journal of the Astronautical Sciences*, Vol. 53, Sept. 2005, pp. 301–316, 10.1007/BF03546355.

[18] M. Murata, I. Kawano, and S. Kogure, "Lunar Navigation Satellite System and Positioning Accuracy Evaluation," Long Beach, California, Feb. 2022, pp. 582–586, 10.33012/2022.18220.

[19] "ADXL359 - Low Noise, Low Drift, Low Power 3-Axis MEMS Accelerometer," Datasheet ADXL359 Rev. 0, Analog Devices, Inc.